Simulations of ultrasonic wave propagation in concrete based on a two-dimensional numerical model validated analytically and experimentally

Ting Yu[a,b,*], Jean-François Chaix[a], Lorenzo Audibert[b], Dimitri Komatitsch[a], Vincent Garnier[a], Jean-Marie Hénault[b]

[a] *Aix Marseille Univ, CNRS, Centrale Marseille, LMA, 13453 Marseille, France*
[b] *Electricity of France Research and Development (EDF R&D), 78400 Chatou, France*

ABSTRACT

Several non-destructive evaluation techniques to characterize concrete structures are based on ultrasonic wave propagation. The interpretation of the results is often limited by the scattering phenomena between the ultrasonic wave and the high concentration aggregates contained in the cement matrix. Numerical simulations allow for further insights. This study aims to build a two-dimensional numerical model in order to reproduce and interpret ultrasonic wave propagations in concrete. The model is built in a spectral-element software package called SPECFEM2D. The validation of the numerical tool is based on the use of resin samples containing different amount of aluminum rods from low (5%) to high concentration (40%), the last one being representative of aggregate concentration in concrete. These samples are characterized using an ultrasonic testing bench (ultrasonic water tank) from 150 kHz to 370 kHz. The measured results are analyzed in terms of phase velocity and attenuation which are the main parameters of coherent waves. As homogenization models such as the Waterman-Truell or Conoir-Norris models are usually used to model coherent waves in two-phase systems, we also compare the experimental and numerical results against them. We confirm that the use of these homogenization models is limited to low concentration of scattering phase, which is not adapted to applications to concrete. Finally, we use our numerical tool to carry out a parametric study on scatterer concentration, shape, orientation and size distribution of aggregates in concrete. We show that aggregate orientation has an influence on coherent wave parameters, but aggregate shape has not.

1. Introduction

Concrete has been used in buildings for many decades and is nowadays one of the most common materials in civil engineering. To optimize the durability and the maintenance of these structures, owners must be able to use experimental techniques to control that their realization conforms to the standards and to assess possible degradation of the materials with time. This is the reason why many Non Destructive Evaluation (NDE) techniques have been developed. Among them, several are based on ultrasonic wave propagation [1].

One phenomenon that is common to any wave propagation study has to be considered: wave scattering in a heterogeneous medium. Three regimes are distinguished, considering the ratio between the wavelength λ and the scatterer size a: Rayleigh, stochastic and geometric regimes. They are commonly characterized by the value of ka, where k is wave number defined by $k = 2\pi/\lambda$. When the wavelength is shorter than the geometric size of the structure but much longer than the aggregate size ($ka \ll 1$, 20–150 kHz for concrete), wave propagation is in the so-called Rayleigh regime and the coherent wave dominates. While the frequency increases, the wavelength is of the order of the aggregate size ($ka \approx 1$ for the frequency range 150 kHz up to 1 MHz for concrete) and wave propagation is in the so-called stochastic regime, meaning that the coherent wave diminishes and that the incoherent wave increases [2,3]. However, coherent wave properties can still be studied by averaging a large number of wave fields. For higher frequencies, in the geometric regime ($ka \gg 1$), ultrasound waves are heavily attenuated and are hardly used in applications.

Linear ultrasonic NDE techniques are used operationally to characterize concrete on site [4–6]. The main analyzed parameters are the coherent wave ones: phase velocity and attenuation [7]. Other techniques based on the analysis of the incoherent waves, also called coda waves, are being developed, but are not yet widely available industrially. In this study we choose to focus on the coherent wave parameters that are strongly linked to the mechanical properties and the ageing of concrete.

In many applications of wave propagation in a scattering media, homogenization theory provides easy-to-use models. The aim of some of these theories [8,17] is to define an equivalent medium which has the same coherent properties as the real heterogeneous system. The developed models are defined in both Rayleigh and stochastic regimes.

* Corresponding author at: Aix Marseille Univ, CNRS, Centrale Marseille, LMA, 13453 Marseille, France.
  E-mail addresses: ting.yu@edf.fr (T. Yu), jean-francois.chaix@univ-amu.fr (J.-F. Chaix), lorenzo.audibert@edf.fr (L. Audibert), komatitsch@lma.cnrs-mrs.fr (D. Komatitsch), vincent.garnier@univ-amu.fr (V. Garnier), jean-marie.henault@edf.fr (J.-M. Hénault).

These models can be separated into two groups: static and dynamic models. The first ones are in direct relation with mechanical properties, but are not able to describe the frequency dependence of wave propagation. The second ones allow for the description of the frequency behavior of the wave parameters. It is worth mentioning that other homogenization approaches, which often imply more involved numerical calculations to obtain a heterogeneous homogenized medium, are available in the literature [18,19].

In these dynamic models the coherent wave has an effective wavenumber which has a complex value. Its imaginary part accounts for attenuation due to scattering in all directions. Foldy [8] first proposed an expression for the effective wavenumber of isotropic point scatterers for scalar waves. Based on this model, numerous subsequent models have been proposed [9–17] to improve the Foldy theory. Among them, the Waterman-Truell model [10], which is commonly used, considers scattering both forward and backward and a second-order correction to Foldy's formula in terms of the scatterer concentration. With the use of the quasi-crystalline approximation (QCA), Vander Meulen [13] introduced the Percus-Yevick equation (QCA-PY) as a spatial pair-correlation function between scatterers. Linton and Martin [14,15] derived the two-dimensional counterpart of Lloyd and Berry's model [12] for spherical scatterers taking into account the boundary effect, as well as the hole correction that is involved in the integral equation to transform volume to surface integrals. Some models rely on one of the previous models and use an iterative process in order to converge toward an equivalent medium, for instance the Generalized Self Consistent Model (GSCM) [16]. For elastic waves, more recently, Conoir and Norris [17] generalized the formulas of Lloyd and Berry's model for reflected and transmitted waves in all the directions in order to take into account mode conversions between pressure and shear waves.

Some researchers have attempted to show the applicability and validity of these models based on experimental comparisons. McClements [20] measured the velocity and attenuation in suspensions of fluid particles in a fluid matrix to compare them with the WT model and Lloyd-Berry model. Good agreement is obtained for both models in a dilute emulsion (volume fraction < 13%). Meulen [13] studied the WT model and the QCA-PY model for suspensions of solid particles in a fluid matrix. In comparison with the experiments at a volume fraction of 3%, good agreement for velocity is obtained for both models. Chaix [21] validated the WT model experimentally in a cement-based medium with air spheres up to 30% with a correction of matrix characteristics (measured velocity and attenuation in the cement matrix).

Most of the experimental validations are performed in the case of a fluid matrix, or of a solid matrix containing air or fluid scatterers, but more rarely in the case of a solid matrix containing solid scatterers. More recently, Chaix [22] compared two homogenization models, the WT model and the GSCM, with the experiments in a cement matrix including elastic or fluid scattering particles. In comparison with the experiments in the cement matrix with 34% of glass beads, the GSCM gives good agreement for velocity and for attenuation at low frequency, while the WT model is less accurate.

However, concrete is a high-concentration scattering medium in the frequency range used in our applications. Considering the possible application of dynamic models to the case of concrete, taking into account the shape and the nature of the scatterers, there is thus lack of knowledge of the limits of these models in terms of scatterer concentration and frequency. This fact leads to the need to resort to full-wave numerical simulations. Moreover, numerical models will overcome other limits of the homogenization models that do not take into account other parameters such as scatterer shapes, the presence of a steel frame, the interfacial transition zone between the scatterers and the matrix, etc.

There are few studies available regarding numerical modeling of ultrasonic wave propagations in concrete [23,24]. Chekroun [23] used simulations performed based on a two-dimensional (2-D) finite difference modelling tool called PROSPERO. He studied the case of identical

circle aggregate scatterers in a cement matrix, up to an aggregate concentration of 60%. He analyzed the results in terms of coherent wave parameters. The numerical results were in agreement for the phase velocity with the Waterman-Truell model up to a scatterer concentration of 10%, and with the Conoir-Norris model up to 25%. Nevertheless, no experimental data were generated to validate the numerical model.

The main objective of this study is thus to develop a 2-D plane strain numerical model in order to predict and interpret ultrasonic wave propagation in concrete, i.e. in a highly-heterogeneous medium. Using a 2-D approximation is currently preferred to 3-D because of its very significantly lower computational cost. Before using this numerical tool for parametric studies, it is necessary to validate it for our application condition: significant heterogeneity. And, as there is a lack of data with a high concentration of solid scatterers in a solid medium, under well-known conditions, an experimental study is mandatory.

This article is thus divided into four parts.

First, we present the experimental setup. We introduce the material properties of concrete and we justify the concentrations of scatterers in our samples by analyzing the aggregate size distribution coming from a real concrete formulation. Several samples of aluminum rods in resin are created to represent a highly-heterogeneous medium like concrete, and characterized in an ultrasonic testing bench from 150 kHz to 370 kHz. The measuring results are analyzed in terms of phase velocity and attenuation, which are the main parameters used to describe coherent waves. The data processing algorithm is presented.

We then present our numerical model. It is developed based on a time-domain spectral-element software package called SPECFEM2D [25]. Additional tools are Matlab codes or Python scripts developed under the Salome platform [26] to generate heterogeneous media. The mesh of the geometry is produced with the TRELIS [27] software package. As our wave sources are wide-band Ricker (i.e., second derivative of a Gaussian) functions, results can be processed to extract coherent wave parameters for each frequency.

The numerical tool is then validated step-by-step. We first consider the simplest case of scattering: a single circular scatterer in a homogeneous matrix. In this configuration, analytical solutions are available in the far field. Then, numerical results are compared to experimental ones in the configurations of the aluminum/resin samples with different concentrations of rods. As homogenization models such as the Waterman-Truell or the Conoir-Norris models are usually used to model coherent waves in two-phase systems, we also compare the experimental results to them.

Finally, we use our validated numerical tool to carry out a parametric study of scatterer concentration, shape, orientation and size distribution of aggregates in concrete.

2. Experimental setup

In this section, the experimental setup for the wave propagation in a highly-heterogeneous medium like concrete is presented. We first recall the properties of the type of concrete that we will use in the parametric studies. We then introduce the measurement samples made of resin matrix with metallic rods, which can represent media with strong heterogeneity such as concrete. Let us note that these samples will be used for all the experiments: analytical, numerical and experimental. Finally, we give the measurement protocol and data processing methodology in order to obtain the effective phase velocity and effective attenuation corresponding to multiple scattering in the samples.

2.1. Concrete properties

Our application concerns ultrasonic wave propagation in concrete. There are many types of concrete with different properties. We choose to set the properties in our numerical study according to the values given in [28]. The mortar is taken as the matrix, and characterized by a
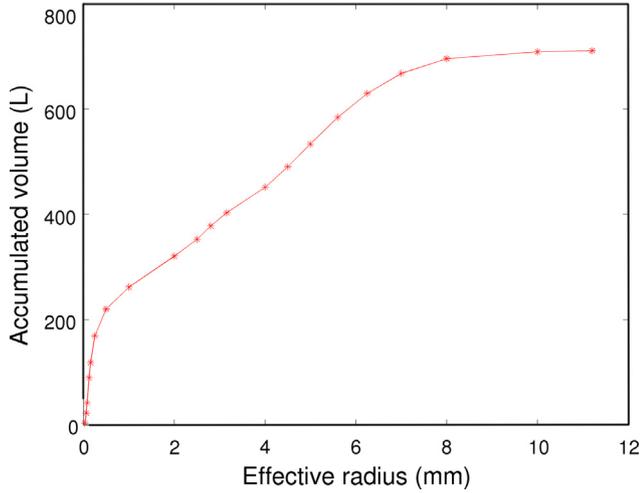
Fig. 1. Size distribution of aggregates for VeRCoRs concrete.

pressure (P) wave velocity $c_{p1} = 3950$ m/s, shear (S) wave velocity $c_{s1} = 2250$ m/s, density $\rho_1 = 2050$ kg/m^3. The aggregate scatterers are characterized by $c_{p2} = 4300$ m/s, $c_{s2} = 2475$ m/s, $\rho_2 = 2610$ kg/m^3. In all the document, the matrix of a heterogeneous medium is labelled 1 and the scatterers labelled 2, while pressure and shear waves are respectively noted as P and S.

Size distribution of scatterers must also be representative of real concrete. We choose to consider information coming from the EDF VeRCoRs project, which is a 1/3-scaled experimental mock-up of a containment building [29]. The aggregate distribution is shown in Fig. 1. In all the document, we note a the radius of the scatterer (radius of the effective circle with the same surface of a noncircular scatterer) and k the wavenumber. A minimal threshold of aggregate size $a \geq 1$ mm is chosen in order to remain around the stochastic regime ($k_{p1}a \approx 1$). The smaller aggregates, which are not taken into account, contribute very little to the scattering phenomenon since $k_{p1}a \ll 1$ (Table 1) and we homogenize them in the mortar. In practice, all the aggregates selected through a sieve of 2 mm are considered in this study and the corresponding volume concentration is 44% for VeRCoRs concrete. This value will be the upper limit of scatterer concentration in our study (see Table 2).

2.2. Sample fabrication

For the experimental measurements, the sample configuration is imposed by the 2-D numerical simulation option that we have chosen. The samples are composed of a homogeneous matrix containing randomly-distributed cylinders. For practical reasons, the samples are not made with concrete components: a resin (polyurethane-polyol) is used as the matrix and rods of aluminum alloy (AlMg5-EM5356 – 95% aluminum and 5% magnesium) with a radius of 0.8 mm are used as scatterers (Fig. 2). The microbubbles in the resin are ignored because of its low-porosity nature. The samples are 7 cm wide and 35 cm long. The length of the rods is equal to the 7 cm width, which is 80 times more than its radius of 0.8 mm, and thus they could be considered as infinites in the Z axis direction. The cross section parallel to the XOY plane is invariant along the Z axis direction, and thus wave propagation in this

Table 1
$k_{p1}a$ for a radius of 1 mm and of 12 mm.

$k_{p1}a$	50 kHz	500 kHz
$a = 1$ mm	0.08	0.80
$a = 6$ mm	0.48	4.77
$a = 12$ mm	0.95	9.54

Table 2
Numerical values for different physical cases.

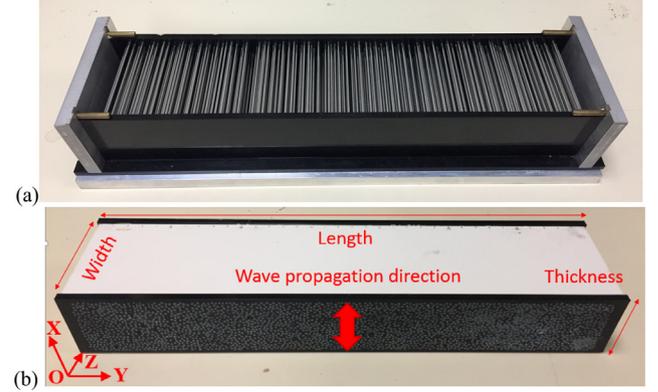| Physical case	N_X	Δd_X (mm)	N_Y	Δd_Y (mm)	N
Concrete (mortar/ aggregates)	100	4	50	12 for circular scatterers of radius 6 mm 8 for other cases	50
Resin/aluminum rods	60	0.8	30	2	30

Fig. 2. Example of one of the samples. (a) Rods in aluminum in the mold before pouring the resin. (b) The same, after the hardening of resin.

cross section can be considered as a 2-D problem.

The material properties are $c_{p1} = 2460$ m/s, $c_{s1} = 1580$ m/s, $\rho_1 = 1600$ kg/m^3 for the resin, and $c_{p2} = 6300$ m/s, $c_{s2} = 3200$ m/s, $\rho_2 = 2700$ kg/m^3 for the rods. We notice that the resin/aluminum acoustic impedance contrast ($\rho_1 c_1 / \rho_2 c_2$ from 23% to 30%) is much stronger than the one between the mortar and the aggregates (about 72%).

The thickness of samples is limited to 5 cm because of the chemical properties of the resin during the pouring (too much heat being generated from the resin hardening reaction). Thus, the considered frequency range starts at 150 kHz, which corresponds to about 3 wavelengths ($\lambda_{p1} = 16.4$ mm at 150 kHz) over the sample thickness of 5 cm. The radius of the rods, 0.8 mm, is determined by $k_{p1}a = 1$ at 500 kHz, corresponding to about 10 wavelengths ($\lambda_{p1} = 4.9$ mm at 500 kHz) over the sample thickness of 5 cm.

The random positions of the rods are analytically calculated with a minimal distance of 0.2 mm so that the scatterer distribution is as homogeneous as possible in the samples. The sample surfaces are polished after resin hardening in order to keep them smooth and with one surface parallel to the other.

Samples with four different scatterer concentrations of 5%, 20%, 30% and 40% are created to study the multiple scattering phenomena. The highest concentration value is representative of aggregate concentration in concrete (44%).

Since the resin is not an elastic material, the velocity and the attenuation of coherent waves are affected by inelastic dispersion in the resin material in addition to the scattering phenomena by the metallic rods. Thus, two samples without rods (with a thickness of respectively 35.0 mm and 49.3 mm) are also created to evaluate and separate the contribution of inelastic dispersion.

2.3. Measurement protocol

An ultrasonic measurement setup (Fig. 3) is developed to obtain the coherent wave across the samples. The measurements are performed in the configuration of P wave transmission in immersion in a water tank. The samples are fixed on a rotatable mount, which allows one to adjust its horizontal and vertical angles, in order for the two largest surfaces of the samples to be parallel to the transducer surfaces and their
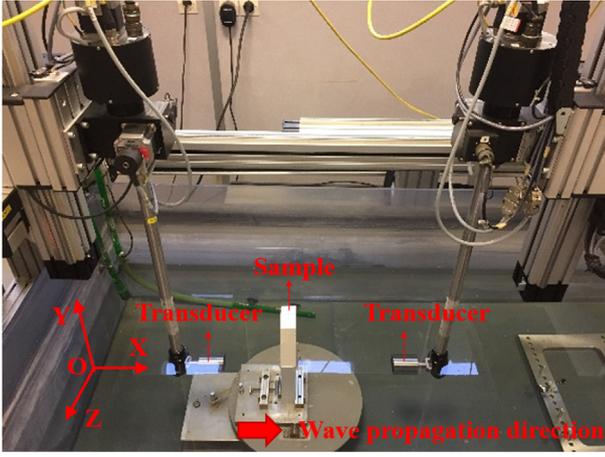
Fig. 3. Ultrasonic experimental setup in immersion in a water tank used in our experiments. The waves propagate along the X axis.

translations. The sample is located in the far field of the transmitter to obtain a stable and reproducible plane wave.

Onepairs of transducers is used: Imasonic 9223–250 kHz with a diameter of 46 mm. Their total passbands are found ranged from 150 kHz to 370 kHz at −6 dB.

The signals are emitted thanks to an impulse generator and received through an amplifier and a digital oscilloscope. For one measurement of any given sample, the transducers target the middle of the sample in its width direction, and 10 acquisitions are recorded along the length direction every 25 mm (Fig. 2(b)). We average these 10 acquisitions as the received signal to obtain the measured coherent wave. We repeated eight times the measurements of the three samples (without rods and with rods at the concentration of 20%) in order to estimate the measurement uncertainty.

Over the frequency range, the received signals after Fourier transform have a maximum amplitude around 300 kHz instead of 250 kHz (the dominant frequency of transducers). This might be linked to the strong impedance contrast between resin and aluminum and a large wave mode conversion. When the wavelength in the matrix of converted S wave is equal to the perimeter of the rods, as $k_{s1}a = 2\pi a/\lambda_{s1} = 1$ at 300 kHz, it might lead the rods to resonate.

2.4. Data processing

The data processing is based on the assumption that the averaged signal represents the measured coherent wave.

If the emitted signal is denoted by $s_0(t)$, the averaged signal $s(t)$ can be expressed as:

$$s(t) = s_0(t) * g_e(t) * e_e(t) * h(d, t) * h_w(D-d, t) * e_r(t) * g_r(t) \tag{1}$$

where $g_e(t)$, $g_r(t)$, $e_e(t)$, $e_r(t)$ are respectively the response functions in the time domain for the generator and the transducers in emission and in reception, $h(d, t)$ is the response function concerning propagation in the sample having a thickness of d, and $h_w(D-d, t)$ is the response function concerning propagation in the water, the distance between two transducers being D.

After a Fourier transform, the averaged signal in the frequency domain is then:

$$\hat{s}(\omega) = \hat{s}_0(\omega) \cdot \hat{g}_e(\omega) \cdot \hat{e}_e(\omega) \cdot \hat{h}(d, \omega) \cdot \hat{h}_w(D-d, \omega) \cdot \hat{e}_r(\omega) \cdot \hat{g}_r(\omega) \tag{2}$$

with

$$\hat{h}_w(D-d, \omega) = e^{i\omega (D-d/c_w)}, \quad \hat{h}(d, \omega) = e^{ik_{sample}(\omega)d} \cdot T_{w/s} \cdot T_{s/w},$$

where $T_{w/s}$, $T_{s/w}$ are respectively the transmission coefficients at the water/sample and sample/water interfaces, c_w is the velocity in the

water, which is assumed to be constant in the frequency range used, and k_{sample} is the complex wavenumber corresponding to the propagation in the sample affected by both inelastic dispersion in the resin and the rods scattering phenomena.

For the coherent wave, we use $\hat{s}(\omega) = A(\omega) \cdot e^{i\phi(\omega)}$. Data processing then relies on two steps.

The first step consists in comparing the results obtained with the resin samples without rods with two different thicknesses, d_1 and d_2. The correction of beam divergence for the transducers is neglected because of the weak difference between the two compared configurations. For these samples, k_{sample} includes only the dispersion in the resin, and can be expressed as $k_{sample} = k_{res} = \omega/c_{res} + i \cdot \alpha_{res}$ with the phase velocity $c_{res}(\omega)$ and the attenuation $\alpha_{res}(\omega)$ of resin. Their expressions are:

$$\alpha_{res}(\omega) = \frac{1}{d_2-d_1}\ln\frac{A_1(\omega)}{A_2(\omega)}, \quad \frac{1}{c_{res}(\omega)} = \frac{1}{c_w} + \frac{\phi_2-\phi_1}{(d_2-d_1)\omega} \tag{3}$$

where A_1 and A_2 are the amplitudes, and ϕ_1 and ϕ_2 are the phases of the measured coherent waves for the two samples without rods.

The second step is performed between a sample without rods (labelled 1 below) and a sample with rods (labelled 2). The correction of beam divergence for the transducers is also neglected for the same reasons. For the sample with rods, the k_{sample} that is present in the response function of the sample represents not only the dispersion in the resin but also the multiple scattering phenomenon. It can be expressed as $k_{sample} = k_{res} + k^*$. Thanks to $c_{res}(\omega)$ and $\alpha_{res}(\omega)$ obtained in (3), the effective parameters corresponding to the effect of multiple scattering phenomenon can be calculated as:

$$\alpha^*(\omega) = \frac{1}{d_2}\left[\ln\frac{A_1(\omega)}{A_2(\omega)} - \alpha_{res}(\omega)(d_2-d_1)\right], \quad \frac{1}{c^*(\omega)} = \frac{\phi_2-\phi_1}{d_2\omega} + \frac{(d_2-d_1)}{c_w d_2}$$
$$- \frac{(d_2-d_1)}{c_{res}(\omega)d_2} \tag{4}$$

By means of the results over the eight repeated measurements of the samples without rods and with rods at the concentration of 20%, the uncertainties within three standard deviations of the means can be reduced at each ω and the maxima over the range from 150 kHz to 370 kHz are ±23.7 m/s for the velocity $c^*(\omega)$ and ±7.0 Np/m for the attenuation $\alpha^*(\omega)$.

3. Numerical model

All the simulations are carried out in the SPECFEM2D software package [25], which is an open-source code for wave propagation in 2-D media in the time domain based upon a spectral-element method.

In the numerical simulation, we evaluate the parameters of $c^*(\omega)$ and $\alpha^*(\omega)$ based on several classical hypotheses:

- viscosity (viscoelastic attenuation) and heat conduction are neglected;
- all the materials inside a given domain are considered homogeneous, linear elastic, and isotropic;
- the scatterers are never in contact (a small exclusion distance is enforced when generating the random media to study);
- the contact at the interface between the matrix and the scatterers is considered perfect;
- wave propagation in 2-D is performed in the plane strain formulation.

3.1. Geometry of the models considered

The 2-D numerical medium that we consider is a rectangular plane consisting of a heterogeneous region $[X \times Y]$ located between two homogeneous matrix regions $[X' \times Y]$ (Fig. 4). Circular or polygonal scatterers are randomly distributed in the heterogeneous region. The
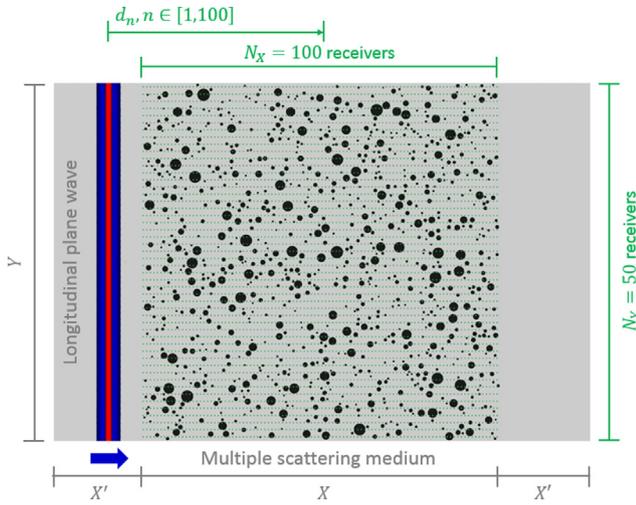
Fig. 4. Example of 2-D numerical configuration in SPECFEM2D for the case of a scatterer concentration of 24%: the black circles represent the circular rods, the green dots the receivers. The receiver positions d_n are defined by the propagating distance of the plane wave, as $d_n = d_{X1} + (n-1) \cdot \Delta d_x$ (d_{X1} the distance between the first receiver in each row and the plane wave at $t = 0$. Δd_X the spacing along the X direction, $n \in [1, N_X]$).

homogeneous region is needed in order to be able to easily generate the initial field for the incident plane wave. Along each edge we enforce an absorbing boundary condition of the Bielak and Christiano [30] type, which is exact for such a plane wave, in order to mimic an infinite medium and avoid spurious reflections coming back from the artificial edges of the domain.

In the simulations of wave propagation in concrete (mortar/aggregates), we define $X = 400$ mm, $Y = 600$ mm for the case with circular scatterers of radius 6 mm, and $Y = 400$ mm for other cases. The length of heterogeneous region in the propagation direction $X = 400$ mm corresponds to about 5 maximum wavelengths over the considered frequency range ($\lambda_{p1} = 79.0$ mm at 50 kHz).

However, in the simulations of wave propagation in resin with metallic rods to compare with the measurements, we adapt the model to the dimensions of the measured samples and we thus define $X = 50$ mm, $Y = 100$ mm. Let us note that the positions of rods are the same as in the samples.

3.2. Wave source

Considering classical aggregate sizes in concrete, a minimum frequency of about 50 kHz corresponds to the stochastic regime in the case of a large aggregate size (effective radius a around 12 mm, Fig. 1), and the upper limit in terms of frequency is about 500 kHz, at which point the coherent wave loses most of its energy and coda (incoherent wave) phenomena become dominant. Consequently, a pressure Ricker (i.e., second derivative of a Gaussian) plane wave with a dominant frequency of 250 kHz is selected as incident wave, most of whose energy is thus distributed over a frequency range of about 50–500 kHz (Fig. 5).

On the other hand, in the simulations of wave propagation in resin with metallic rods, a pressure Ricker plane wave with a dominant frequency of 300 kHz is selected as incident wave. In order to reduce the total number of simulations to perform, the choice is adapted to the observed energy concentration around 300 kHz of received signals in the measurements, in order to explore a frequency range as large as possible (cf. Section 2.3).

3.3. Mesh, accuracy of the numerical calculations, and numerical stability

Mesh generation is performed using quadrangular elements in the commercial software package TRELIS [27]. A quadrilateral element

type with second-order polynomial shape functions and thus with nine geometrical control nodes, often called QUAD9, is used to describe the curved interfaces. The average mesh size Δl must comply with two conditions: (1) $\Delta l \leq \lambda$ (wavelength $\lambda = c/f$) for numerical accuracy of wave propagation based on the spectral-element method [31], and (2) accurate geometrical description of the smallest scatterers (for example, aggregate scatterers of $a = 1$ mm in the concrete case and rods of $a = 0.8$ mm in the resin/aluminum case). We have thus performed a numerical convergence study in order to determine the mesh size needed and verify compliance with these two conditions. Moreover, mesh quality was checked in terms of size and element skewness before each simulation.

The time step Δt needed for these explicit, time-domain, conditionally-stable simulations is linked to the minimal mesh size in accordance with the Courant-Friedrichs-Lewy (CFL) stability condition: $\Delta t \cdot \max(c/\Delta l) \leq n_{CFL}$, where n_{CFL} is a constant that is about 0.5 in the case of explicit 2-D spectral-element techniques in heterogeneous media [31].

3.4. Data processing

A set of sensors (receivers) that record displacement is placed in the heterogeneous medium region $[X \times Y]$ in order to record the wave field (Fig. 4): N_X receivers along the X direction with an even spacing of Δd_X, and N_Y rows of receivers with row spacing Δd_Y in the Y direction.

In order to compare with the homogenization models and monitor the wave propagation, we choose the same effective parameters, phase velocity and attenuation. They could be obtained from the direct numerical results in terms of displacements by the following data processing.

The coherent field of scattered P waves $s(t, d_n)$ is obtained by averaging the displacements in the X direction of N signals at position d_n, and it is then processed by Fourier Transform:

$$s(t, d_n) \xrightarrow{FT} \hat{s}(\omega, d_n) = A(\omega, d_n)e^{i\phi_n(\omega)} \tag{5}$$

where $\hat{s}(\omega, d_n)$ is the coherent field in the frequency domain at position d_n, and A and ϕ_n are respectively the amplitude spectrum and the phase spectrum at position d_n.

The attenuation α^* of the coherent field can be obtained by measuring the change of the amplitude spectrum, which is assumed to decrease exponentially with propagation distance as in a homogeneous medium:

$$A(\omega, d_n) = A_0(\omega)e^{-\alpha^* d_n} \tag{6}$$

where $A_0(\omega)$ is the initial amplitude of the wave source at ω. Even though the attenuation can be calculated based on the amplitudes recorded at two positions by using the expression $\alpha^* = \ln[A(d_m)/A(d_n)]/(d_n - d_m)$, the final value is obtained by curve fitting based on the amplitudes measured at all the positions, in order to increase the accuracy of the attenuation estimated.

In order to obtain the effective phase velocity of the coherent field, we use the $p-\omega$ transform method [32]. In that method, a summation function is defined as:

$$F(p, \omega) = \sum_{n=1}^{N_X} \frac{e^{i\phi_n(\omega)}}{e^{i\phi_1(\omega)}} e^{i\omega p d_n}, \tag{7}$$

where p is the slowness of the propagating wave in the matrix, $p = 1/c$.

For a given angular frequency ω, the summation function is calculated based on a group of different values for p over the range from $1/c_{p1}$ to $1/c_{p2}$. The phase velocity of the coherent wave c^* then corresponds to the p ($p = 1/c$) that gives the maximum of $F(p, \omega)$.

A convergence study is carried out to determine N, the number of averaged signals that is needed to obtain the coherent field. We have used 500 rows of receivers in the simulations of 10 different configurations, in which circular scatterers of identical radius 6 mm at a
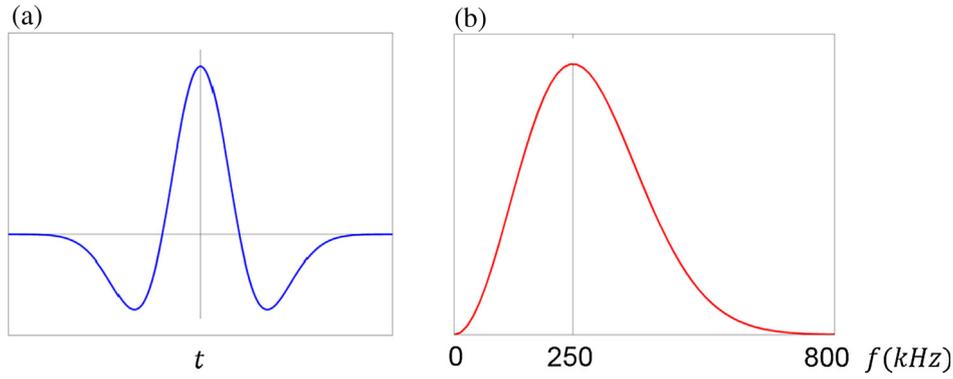
Fig. 5. Ricker (i.e., second derivative of a Gaussian) wave with a dominant frequency of 250 kHz in the time domain (a) and its corresponding amplitude spectrum in the frequency domain (b).

concentration of 12% are randomly and differently distributed. We then compare the phase velocity and attenuation obtained based on the averaged fields from 50 rows and 450 rows. The comparisons show that the curves corresponding to 50 rows are close to those corresponding to 450 rows, whose curves are however a bit smoother. The maximal differences between the cases with 50 rows and with 450 rows are 2.5 m/s for the phase velocity and 0.2 Np/m for the attenuation over the range from 50 kHz to 500 kHz. Therefore, $N = 50$ is then used to obtain the coherent field in order to reduce the computational cost.

4. Numerical model validation

The aim of this section is to validate the numerical model in a step-by-step procedure. First, we consider the simplest case of scattering: a single circular scatterer in a homogeneous matrix. In this configuration, analytical solutions are available in the far field. Numerical results are then compared to experimental ones in the configurations of the resin/aluminum samples. Two homogenization models, the Waterman-Truell and Conoir-Norris models are also compared and discussed.

4.1. Scattering by a single circle

In a 2-D plane, in the case of plane strain, an ultrasonic harmonic plane wave at the pulsation $\omega = 2\pi f$ (frequency f) propagating in an elastic matrix, and its interaction with an elastic circle of radius a can be described based on a modal representation of the wave field. The propagation media in the matrix and in the circle are characterized respectively by P wave velocities c_{p1}, c_{p2}, S wave velocities c_{s1}, c_{s2}, and densities ρ_1, ρ_2. The wavenumbers for the P and S waves in the matrix are defined respectively by $k_{p1} = \omega/c_{p1}$, $k_{s1} = \omega/c_{s1}$. Using the far-field approximation $k_{p1}r \gg n$, $k_{s1}r \gg n$ (the distance of observation being r, the mode order integer $n \in [0, +\infty]$), the scattering pattern functions in the matrix for an incident harmonic plane wave in the frequency domain with unit amplitude can be expressed as follows [33,34]:

$$\text{P wave} \begin{cases} f_{pp1}(\theta, \omega, a) = \frac{1-i}{\sqrt{\pi k_{p1}}} \sum_{n=0}^{+\infty} \epsilon_n a_n \cos n\theta \\ f_{ps1}(\theta, \omega, a) = \frac{i-1}{\sqrt{\pi k_{s1}}} \sum_{n=0}^{+\infty} \epsilon_n b_n \sin n\theta \end{cases}, \text{S}$$

$$\text{wave} \begin{cases} f_{sp1}(\theta, \omega, a) = \frac{i-1}{\sqrt{\pi k_{p1}}} \sum_{n=0}^{+\infty} \epsilon_n c_n \sin n\theta \\ f_{ss1}(\theta, \omega, a) = \frac{1-i}{\sqrt{\pi k_{s1}}} \sum_{n=0}^{+\infty} \epsilon_n d_n \cos n\theta \end{cases} \tag{8}$$

where f_{pp1}, f_{ss1} are the scattering pattern functions of the scattered wave without mode conversion in the matrix, and f_{ps1}, f_{sp1} the scattering pattern functions of the converted wave in the matrix. ϵ_n is the Neumann factor with $\epsilon_0 = 1$ and $\epsilon_n = 2$ for $n > 0$. a_n, b_n, c_n, d_n are nth-order modal expansion coefficients for the scattered and converted waves in the matrix. θ is the angle in cylindrical coordinates, and the incident wave propagation direction is defined as $\theta = 0$, while $\theta = \pi$ is

the direction of back-scattering. In this study we use 20 as the maximum value of n to consider only the first 20 modes in the series in Eq. (8), because we have validated that such a value is sufficient for convergence and stability of the calculation of the scattering function.

The scattering cross-section is commonly used to represent the energy distribution after scattering in terms of the scattering direction:

$$\sigma_{type,1}(\theta) = |f_{type,1}(\theta)|^2 \tag{9}$$

For the numerical simulations, we consider a Ricker pressure plane wave with a dominant frequency of 250 kHz scattered by a single circle of radius $a = 6$ mm in a homogeneous medium (Fig. 6). The material properties are those of concrete presented in Section 2.1. The acquisition setup is modified to adapt it to scattering pattern functions that depend on the scattering angles. The receivers are located at the distance of r from the center of the scatterer, at discrete angular positions θ, limiting ourselves to the range $0° \leq \theta \leq 180°$ only because the problem is symmetrical. The angular distance between two successive receivers is $\Delta\theta = 2°$. A distance $r = 200$ mm was chosen based on a convergence study in order to be in the far-field approximation regime, which imposes that $k_{p1}r \gg n$, $k_{s1}r \gg n$. That distance leads to $k_{p1}r = 80$ and $k_{s1}r = 140$ far greater than 20 which is the chosen maximum value of n, at $f = 250$ kHz, thus satisfying the far-field condition. The calculated radial and tangential displacements represent respectively the scattering patterns of scattered P waves and of converted S waves for a Ricker wave.
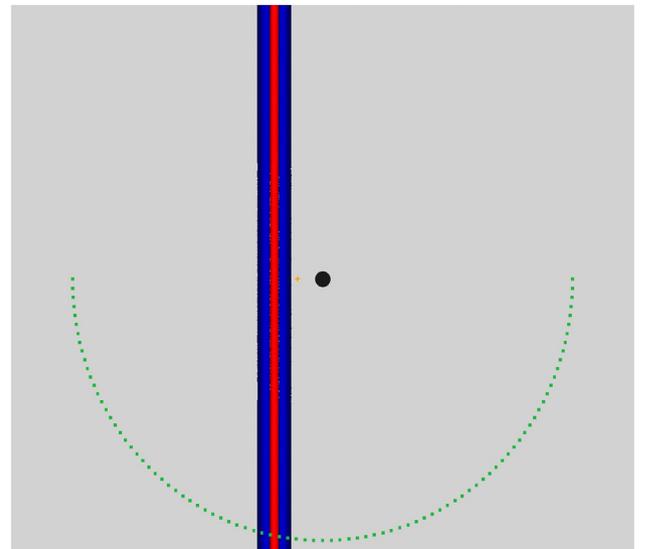

Fig. 6. Sketch of our numerical experiment to study elastic scattering by a single aggregate circle in a cement homogeneous matrix.
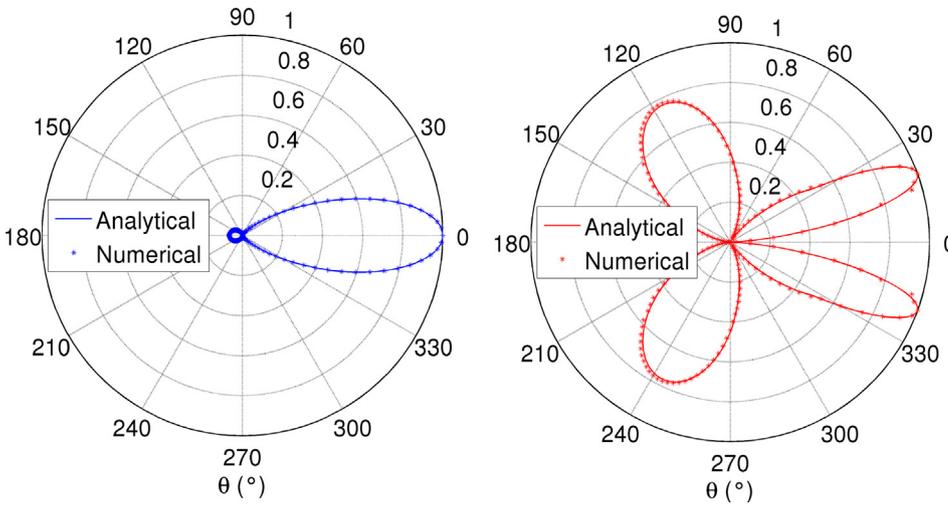
Fig. 7. Analytical (in solid lines) versus numerical (in dashed lines) comparisons of scattering cross-sections of the diffracted P waves (in blue) and the converted S waves (in red) for elastic scattering of a pressure Ricker plane wave with a dominant frequency of 250 kHz by a single circle of radius 6 mm. (For interpretation of the references to colour in this figure legend, the reader is referred to the web version of this article.)

The analytical scattering patterns for a Ricker wave with a dominant frequency of 250 kHz are approximated based on a weighted sum: after a Fourier transform of the Ricker wave, 60 discrete frequencies are taken over the frequency range 0 to 800 kHz, and then the scattering pattern functions in (8) at each discrete frequency $f = \omega/2\pi$ are weighted by the corresponding amplitude and phase and finally summed.

We have calculated the scattering cross-sections from the scattering patterns for both the numerical results (at $r = 200$ mm) and the analytical solution (at infinite distance). Their amplitude at each θ is normalized by the maximum amplitude to highlight the energy distribution after scattering that we are interested in. The comparison is shown in Fig. 7. The curves are superposed and the excellent agreements validate the numerical tool SPECFEM2D for such an application.

4.2. Multiple scattering

4.2.1. Comparison between experimental and numerical results

For comparison with the experimental measurements, we simulate numerically wave propagation in all the configurations described in Section 2.2. We use the exact positions of the rods, which were fixed before creating the samples. We simulate a 100 mm × 50 mm region of the samples. The incident wave is a Ricker pressure plane wave with a dominant frequency of 300 kHz, corresponding to the maximum amplitude of the experimental signal (Section 2.3). Data processing described in Section 2.4, is used to obtain the phase velocity and the attenuation corresponding to multiple scattering from the numerical results.

The comparison in terms of the variation of velocity and attenuation with frequency between experimental results and numerical simulations at all the scatterer concentrations of 5%, 20%, 30% and 40% is shown in Fig. 8.

Regarding the phase velocity in Fig. 8(a), the numerical and experimental results almost remain constant and exhibit a quantitative agreement at a scatterer concentration of 5% in spite of a small difference over the whole frequency range going from 150 kHz to 370 kHz. For scatterer concentrations of 20%, 30% and 40%, the numerical results exhibit a monotonous decaying behavior with respect to frequency, qualitatively similar to what is observed in the experiments. However, the simulations overestimate the velocity values compared to experimental ones, and this underestimation tends to increase with scatterer concentration.

Regarding attenuation, the experimental curves cross each other in the frequency range going from 150 kHz to 370 kHz and exhibit significant experimental uncertainties, especially at low frequency (< 270 kHz) (Fig. 8(b)). At high frequency (> 270 kHz), the strongest

attenuation is observed at a scatterer concentration of 20%, and the attenuation at concentrations of 30% and 40% are close in amplitude, the latter being slightly smaller. We observe a similar phenomenon in the numerical results of Fig. 8(c), where error bars of the experimental results are removed for clarity. However, for all the scatterer concentrations, the numerical simulations underestimate attenuation compared to the measurements, and the differences are almost constant over the frequency range. The differences are smaller at a scatterer concentration of 5% than at 20%, 30% or 40%. For the lowest percentage of scatterers, the agreement is quantitative because the numerical values are included in the uncertainty range of the experimental one. For the other concentrations, the agreement is only qualitative.

These differences between the experiments and the numerical simulations could be explained by two reasons. The first one is that the material properties are not correctly evaluated for the simulations. Secondly, the differences are maybe due to imperfect bonding at the interfaces between the resin and the rods in the experiments, while bonding is assumed to be perfect in the numerical simulations. To be more specific, the resin/air coupling appears at the imperfect bonding and its acoustic impedance is extremely strong. It prevents the waves from propagating directly through aluminum rods where the wave velocity is faster than in resin, and it leads to more scatterings in all the directions. The imperfect bonding thus results in a smaller effective phase velocity and a stronger attenuation than perfect bonding in the simulations.

The relative variations of phase velocity and attenuation can be considered as identical between numerical and experimental results. Therefore the comparisons validate the numerical model and confirm that it permits a good description of multiple scattering phenomena in such a highly-heterogeneous medium.

4.2.2. Comparison with homogenization models

Let us first briefly recall the Waterman-Truell (WT) and Conoir-Norris (CN) homogenization models.

In order to describe wave propagation in a heterogeneous medium having multiple scatterers, homogenization principles suggest to focus on the propagation of the coherent wave, which is the statistical average based on all possible configurations of the scatterers. This defines an equivalent homogeneous attenuating medium corresponding to the coherent wave propagation, and the medium is dispersive with a complex effective wave number k^* that is frequency dependent:

$$k^*(\omega) = \frac{\omega}{c^*} + i \cdot \alpha^*,$$

(10)

where $c^*(\omega)$ is the effective phase velocity and $\alpha^*(\omega)$ the effective
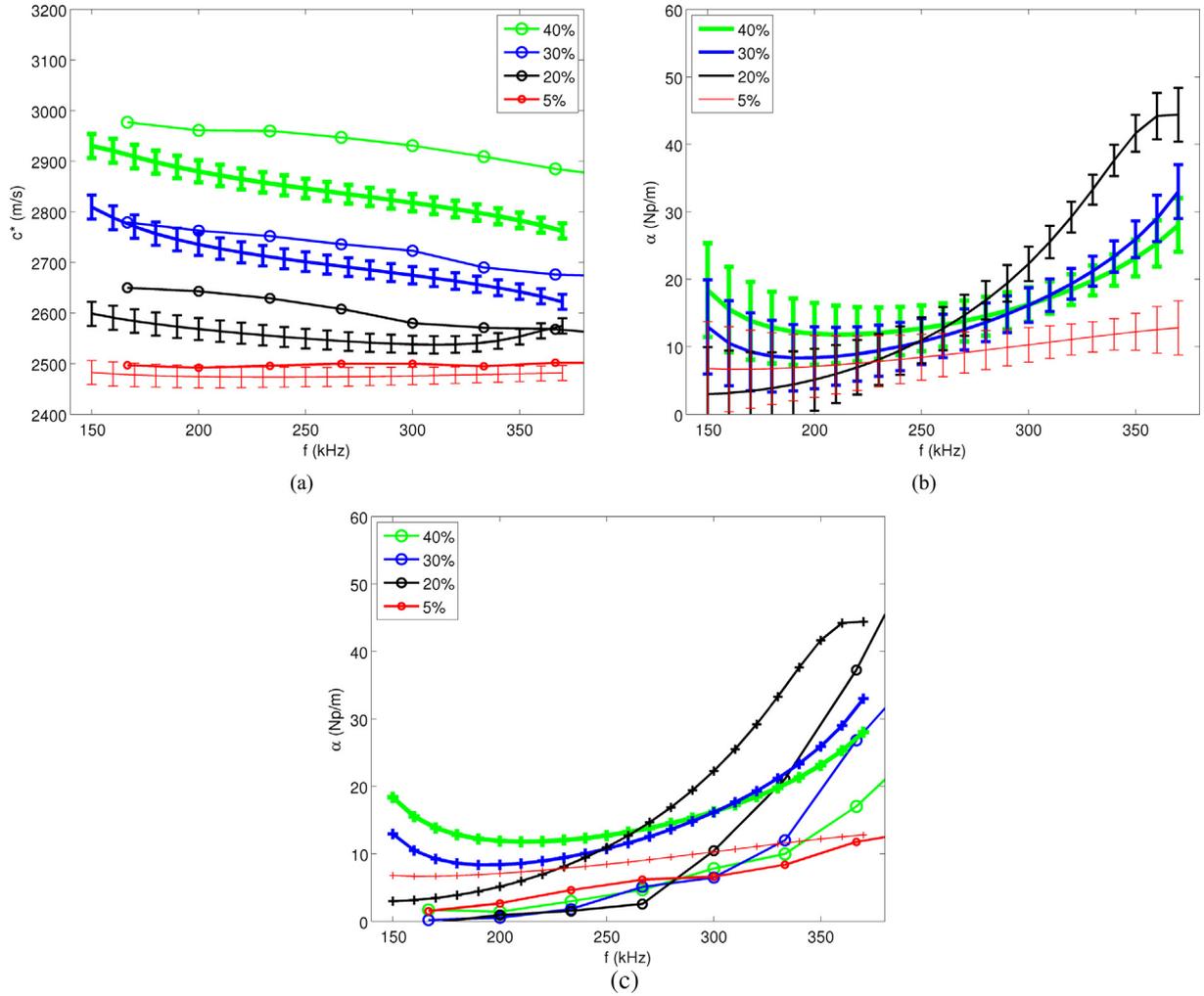
Fig. 8. Experimental (solid line with error bars or crosses) and numerical (solid line with circles) (a) velocity and (b)&(c) attenuation with respect to frequency in the case of pressure wave propagation in a medium composed of 5%, 20%, 30% and 40% of rods in resin. The measured attenuations in (c) are the same as the ones in (b), with the error bars removed for clarity.

attenuation.

The Waterman-Truell (WT) model is a homogenization model that considers forward and backward scattering based on scattering pattern functions. In the case of an incident P wave at ω scattered by identical circles of radius a, it gives the expansion expression of k^* up to second order in the concentration as follows [10]:

$$(k_p^*)^2 = k_{p1}^2 + \delta_1 n_0 + \delta_2 n_0^2 \tag{11}$$

with

$$\delta_1 = \frac{4\sqrt{\pi k_{p1}}}{1+i} f_{pp1}(0), \quad \delta_2 = -\frac{2\pi \cdot i}{k_{p1}}([f_{pp1}(0)]^2 - [f_{pp1}(\pi)]^2)$$

where $n_0 = v/\pi a^2$ is the number of scatterers per surface unit, v is the scatterer concentration and n_0 is supposed to be constant if scatterers are homogeneously distributed.

If scatterers are of different sizes, the WT model can take the size distribution into account by replacing $f(\theta)$ with the effective scattering pattern $\langle f(\theta) \rangle$:

$$\langle f(\theta) \rangle = \int_a f(\theta, a) \cdot p(a) \, da \tag{12}$$

where a is the radius of the scatterers and $p(a)$ is their size distribution.

The LM model [14] provides, based on Loyd and Berry model [12], a mathematical proof of its validity and the new value of δ_2, coefficient

of second order in the concentration. The Conoir-Norris (CN) model builds on the LM model by incorporating mode conversation effects. These effects induce the following modification of the second-order correction term [17]:

$$\delta_2 = \frac{4i}{k_{p1}} \int_0^\pi d\theta \cot\left(\frac{\theta}{2}\right) \frac{d}{d\theta}[f_{pp1}(\theta)f_{pp1}(-\theta)]$$
$$+ 4i\sqrt{k_{p1}k_{s1}} \int_0^\pi d\theta \frac{f_{ps1}(\theta)f_{sp1}(-\theta) + f_{ps1}(-\theta)f_{sp1}(\theta)}{k_{s1}^2 - 2k_{p1}k_{s1}\cos\theta + k_{p1}^2} \tag{13}$$

For the calculation of δ_2, in practice, we used the initial expression in [17] as following:

$$\delta_2 = -\frac{16}{k_{p1}^2} \sum_{m,n} D_{m-n}^{(0)}(k_{p1}) T_m^{pp} T_n^{pp} - \frac{8i\pi}{k_{p1}^2 - k_{s1}^2} \sum_{m',n'} N_{m'-n'}^s(k_{p1}) T_m^{sp} T_n^{sp} \tag{14}$$

where m, n, m', n' are integers, $T_i^{\alpha\beta}$ is the i-th modal scattering amplitudes with $\alpha, \beta \in [p, s]$ representing the wave mode in Fourier series of the scattering pattern functions $f_{\alpha\beta}(\theta)$ in the T-matrix approach, the functions $D_i^{(0)}$ and N_i^s are defined in [17] by using Hankel and Bessel functions.

Let us first compare the experimental results with the results obtained using the WT model and the CN model (Fig. 9).

Regarding phase velocity (Fig. 9(a)), the two models overestimate the velocity compared to the experiments (solid lines with error bars) for all the scatterer concentrations. At a concentration of 5%, the two
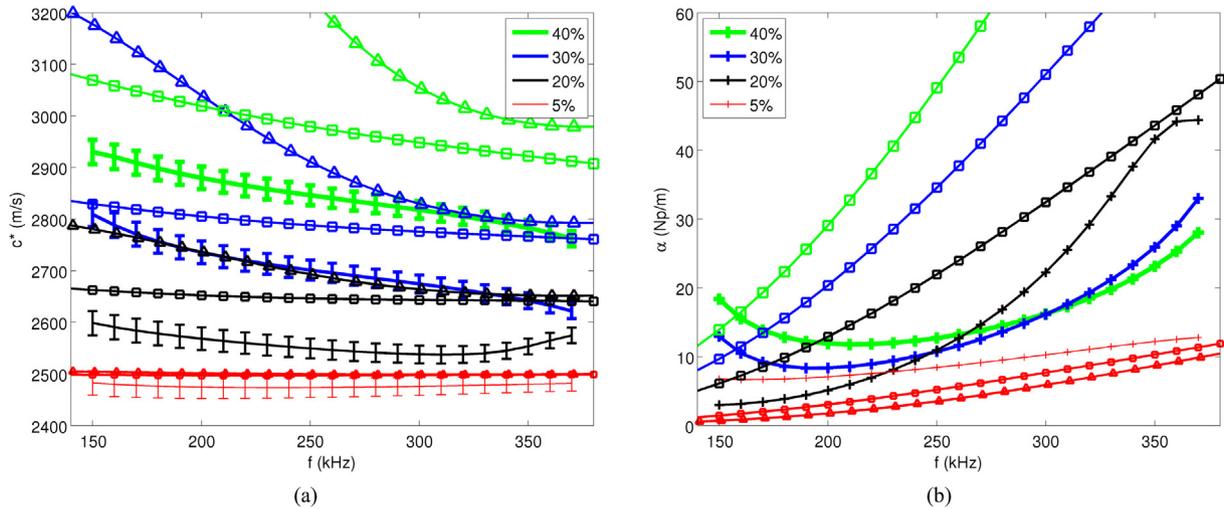
Fig. 9. Experimental (solid lines with error bars or crosses) versus homogenized velocity and attenuation with respect to frequency (solid lines with squares for the WT model and solid lines with triangles for the CN model) in the case of pressure wave propagation in a medium composed of 5%, 20%, 30% and 40% of rods in resin.

models almost overlap and exhibit a good agreement with the experiments in spite of a small difference over the whole frequency range going from 150 kHz et 370 kHz. For the other scatterer concentrations, the WT model (solid line with squares) predicts similar decaying behavior with respect to frequency as observed in the experiments, except in the case of 30% concentration, and the difference between the WT model and experiments increases with scatterer concentration. The CN model (solid line with triangles) leads to a decaying behavior that is much more important than for the WT model, and differs more from the experiments.

Regarding attenuation (Fig. 9(b)), only the results at a concentration of 5% are shown for the CN model (solid lines with triangles) because attenuation at other concentrations obtained by this model is negative, which is unphysical, and which thus means that the model fails. For a concentration of 5%, both models exhibit similar curves as the experiments (solid lines with crosses) and their values are globally smaller over the whole frequency range. The WT model (solid lines with squares) performs better, leading to a smaller difference with the experiments. For scatterer concentrations between 20% and 40%, nevertheless, the attenuation predicted by the WT model is greatly over-estimated compared to the experiments and increases with scatterer concentration, while in experiments the attenuation at a scatterer concentration of 20% is the strongest.

According to the analytical versus experimental comparison, we can thus confirm the quantitative validity of the WT model in our case of solid scatterers in solid matrix at a concentration of 5%, which is in the range of validity limit suggested, and the CN model performs similarly to the WT model at a concentration of 5%, but not above.

In comparison with the experimental results of wave propagation in resin with aluminum rods, these homogenized models are unable to predict phase velocity and attenuation of multiple scattering in a highly-heterogeneous media such as concrete, while full-wave numerical simulations can overcome these limits; for such media it is thus necessary to switch to such numerical tools.

5. Parametric study for concrete cases using the numerical model

For the continuation of this work, we accept that the numerical model allows a qualitative description of the evolutions of the phase velocity and the attenuation in case of scatterer concentration up to 40%, which is representative of applications to concrete. We can now use it to perform a parametric study of ultrasonic wave propagation in a heterogeneous medium. We will first consider the case of concrete containing aggregates with a circular shape, in order to study the influence of scatterer concentration. We will then use polygonal shapes for scatterers to investigate the impact of scatterer shape (comparing the results with those obtained for the case of a circular shape) and of their privileged direction. We will finally compare and discuss results for different size distributions of circular scatterers.

5.1. Scatterer concentration of circular scatterers

The numerical model being validated qualitatively, let us now study the influence of scatterer concentration in the case of circular scatterers. Two cases are simulated: identical circles, and circles of various radii. In the case of identical circles, a radius of $a = 6$ mm is chosen for the concrete aggregates because it is the mean size value observed in VeRCoRs concrete, in which aggregate sizes typically range between 1 and 11 mm. The size distribution in the case of various circles is obtained as follows: in an infinite 3-D volume containing spheres whose radii correspond to the aggregate size distribution of VeRCoRs concrete (Fig. 1), the probability of a circular radius exceeding 1 mm in a random cut plane can be calculated, and then we take it as the size distribution that we will use (dotted line in Fig. 10). The circle locations are chosen randomly in the region $[X \times Y]$, enforcing a minimal exclusion distance between the circles of $\Delta \geq 0.5$ mm.

For each case, we simulate the propagation of a Ricker pressure plane wave with a dominant frequency 250 kHz in a mortar containing 12%, 24% or 42% of circular scatterers. The numerical results are post-processed to obtain the effective phase velocity and attenuation with respect to frequency (cf. Section 3.4).

In the case of identical circles (Fig. 11), the increase in scatterer concentration leads to an increase in the velocity and attenuation values in the whole domain. Regarding phase velocity (Fig. 11(a)), amplitude variations are observed in the low frequency domain ($f \leq 200$ kHz), and the magnitude of variations increases with scatterer concentration. The maxima are found around $k_{p1}a = 1.4$ ($f = 150$ kHz). Then, in the high-frequency domain ($f \geq 200$ kHz), the velocity remains almost constant. Regarding attenuation (Fig. 11(b)), two bumps are observed at about $k_{p1}a = 1.2$ ($f = 130$ kHz) and $k_{p1}a = 3.2$ ($f = 340$ kHz) respectively, and become more obvious as the scatterer concentration increases. This might be linked to the presence of numerous spaces of similar sizes between the identical circles. Even though the scatterer positions are randomly distributed, this comes from the fact that the arrangement of scatterers becomes increasingly closer to a periodic arrangement as the concentration of scatterers increases for a
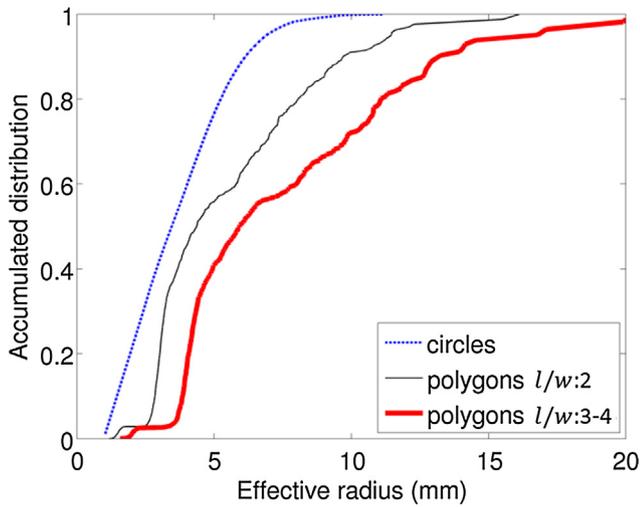
Fig. 10. Size distributions for the numerical cases with circles (dotted line) and polygons with a ratio l/w of about 2 (black solid line) and of about 3–4 (red solid line). l/w is defined by the ratio of the longest dimension of a polygon and the largest width in its perpendicular direction. (For interpretation of the references to colour in this figure legend, the reader is referred to the web version of this article.)

region of finite size.

In the case of circles of various radii (Fig. 12), smoother curves are observed in comparison with the previous case of identical circles only: the amplitude variations at low frequency for the velocity and the two bumps for attenuation disappear. This confirms the previous explanation that the amplitude variations and the bumps are linked to the presence of numerous spaces with similar sizes between the identical scatterers. Regarding phase velocity (Fig. 12(a)), an increase with frequency is observed over the whole frequency range, and the slope becomes steeper with scatterer concentration. Attenuation (Fig. 12(b)) exhibits a quasi-monotonous increase with respect to frequency, and a nearly linear dependence on scatterer concentration in the frequency domain above 200 kHz.

5.2. Scatterer shape and privileged direction: circular versus polygonal scatterers

In the literature, studies have often applied the shape simplification of using circular shapes only to represent scatterers. In order to

investigate the effect of scatterer shape and privileged direction on wave propagation, in this section we will use scatterers of circular shape, and then scatterers of polygonal shape.

In the case of polygonal scatterers, the geometry is generated by extracting a cut plane from a 3-D model of a concrete block with polyhedral aggregates: some polyhedra with a controlled shape (i.e. length/width ratio, l/w) and orientation are generated, with their inscribed sphere radii corresponding to the aggregate size distribution of concrete. Their center is then placed randomly in the cut plane, using a minimal exclusion distance between the polyhedra of $\Delta \geq 0.5$ mm. The polygons in the cut plane are then used as scatterers in the simulations.

In order to highlight the effects of scatterer shape, we simulate two cases for polygons: usual shapes with l/w about 2 (Fig. 14(a)), and exaggerated shapes with l/w about 3–4 (Fig. 14(b)). The former shape is closer to the shape of observed aggregates in a real cut section of VeRCoRs concrete. The scatterer concentrations are respectively 44% and 42%, i.e. slightly different, because it is difficult to control the concentration very precisely when the geometry is numerically generated. The size distributions of effective radii from circles with the same surface as that of the respective polygons is shown for the two cases in Fig. 10.

In the study of the influence of scatterer shape, the simulation of each polygonal case is compared with a corresponding simulation with circular scatterers, and each circle corresponds to a polygon having the same surface. It is impossible to place all the circles at the same positions as the corresponding polygons, and thus they are instead randomly positioned, nonetheless obtaining the same concentrations.

The results for velocity and attenuation are shown in Fig. 14. For both polygonal shapes with l/w of about 2 and of 3–4, the velocity curves exhibit a good agreement with the corresponding simulations performed with circles, and a similar shape of the velocity curve is found, with a small difference coming from the slight concentration difference. Regarding attenuation, the shapes of the curves versus frequency are close for the two polygonal cases. The first bump appears again, and is clearer in the corresponding simulations with circles. This might be linked to size concentrations (many scatterers of a similar size) that show up as significant slopes on the size distribution lines. For polygons with l/w about 3–4 (red line) and with l/w about 2 (black line in Fig. 10), the size concentrations are observed around effective radii respectively of 4 mm and 3 mm. The case of the circular shape appears to be much more sensitive to the size distribution than the case of the polygonal shape regarding attenuation. This likely comes from the fact that the regular shape of circles makes it more probable to create similar intervals between the scatterers when there is a privileged size.
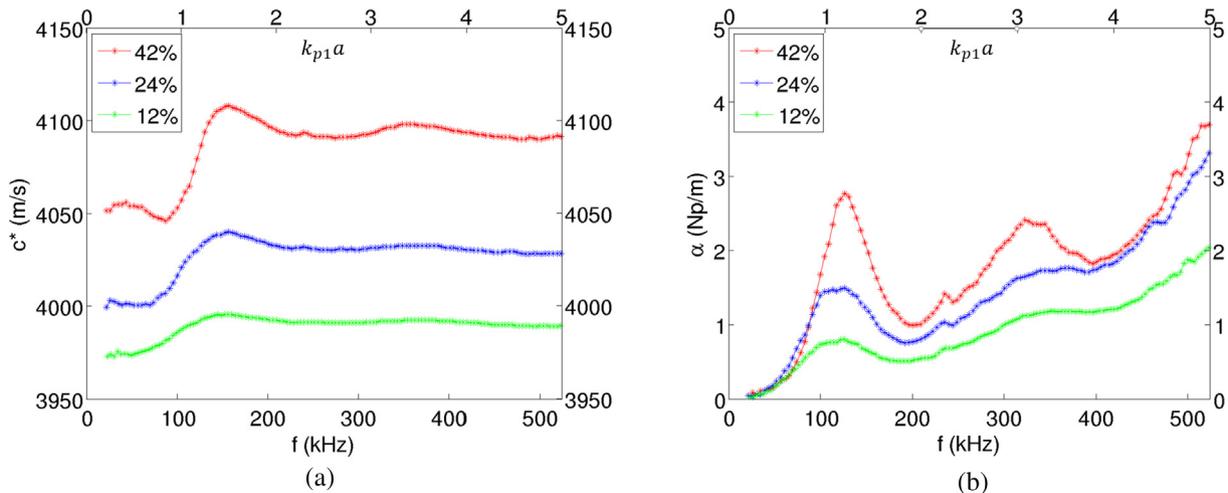

Fig. 11. Variations of velocity and of attenuation versus frequency and versus $k_{p1}a$ in the case of an incident pressure wave propagating in a mortar containing 12%, 24% or 42% of scatterers of radius 6 mm in the case of full-wave numerical results.
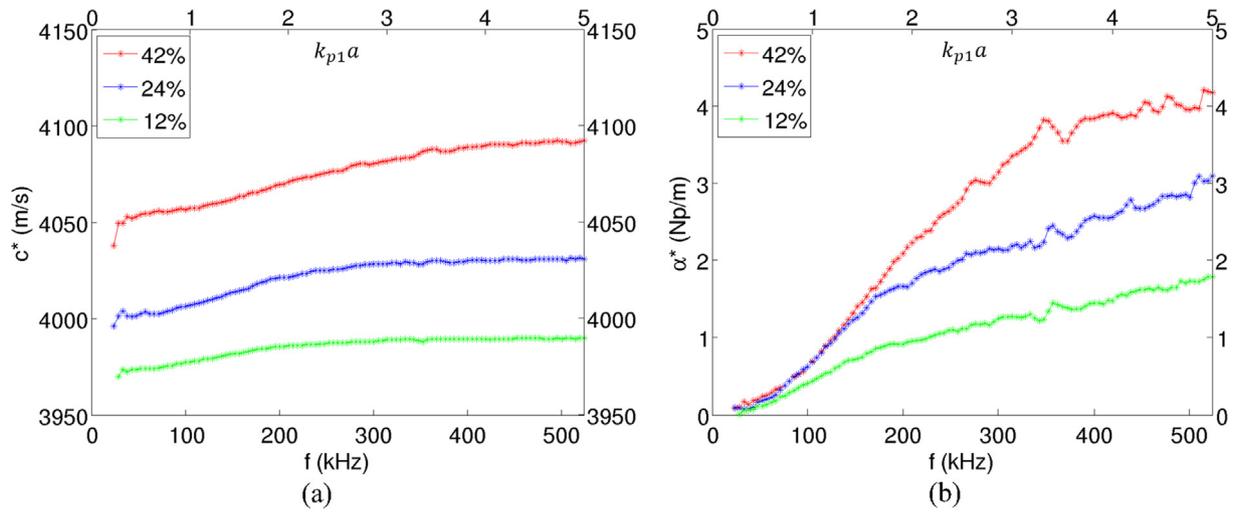
Fig. 12. Variations of velocity and of attenuation versus frequency and versus $k_{p1}a$ in the case of an incident pressure wave propagating in a mortar containing 12%, 24% or 42% of scatterers of various radii in the case of full-wave numerical results.

The circular shape gives a better description of velocity and attenuation versus frequency for the polygonal shape at l/w about 2 than at l/w about 3–4.

Let us now analyze the influence of the direction of the polygons in relation to the direction of the propagating incident plane wave. We apply privileged directions of 0°, 45° and 90° with respect to the wave propagation direction to the case with polygons of exaggerated shape (Fig. 13(c), (d) and (e)). The comparisons are presented in Fig. 15. Regarding velocity, a very similar behavior between the cases with polygons of random directions and a privileged direction of 45° is observed. When the length direction of the polygons is the same as that of the incident wave propagation (case of 0°), there are fewer interfaces along the same propagation distance, and a faster velocity is obtained.

We observe the opposite behavior in the case with a privileged direction of 90°: a slower velocity is obtained because of the presence of more interfaces. But the velocity in all four cases tends to converge to the same value as frequency increases. Similar conclusions are found for attenuation versus frequency. The opposite influence of interfaces regarding attenuation leads to larger amplitude for the case with a privileged direction of 90°, and smaller amplitude for 0° than those for 45° as well as those for random directions. In general, attenuation appears to be more sensitive to privileged directions.

5.3. Size distribution: case of circular scatterers

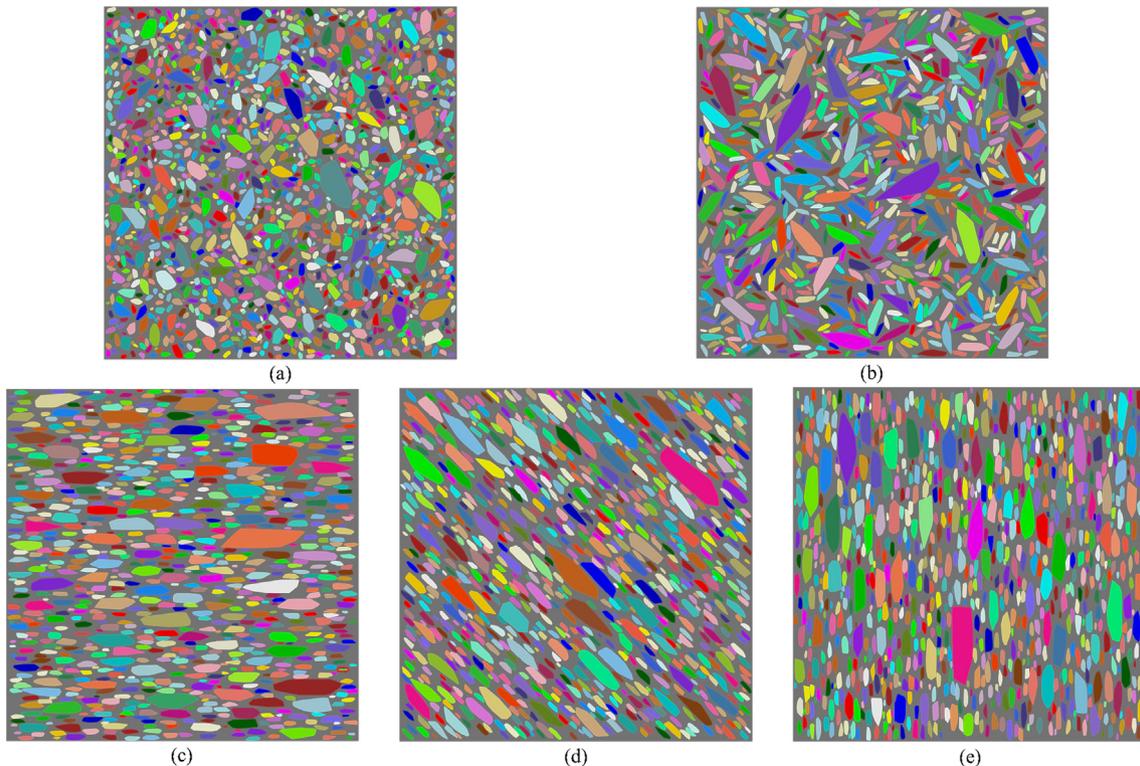The above simulations have four different size distributions of

Fig. 13. Geometry of the mortar containing scatterers of polygonal shape. Polygons with a length over width ratio l/w of 3–4 with random directions (a), with a privileged direction of 0° (b), 45° (c) and 90° (d), and with a length over width ratio l/w of about 2 with random directions (e).
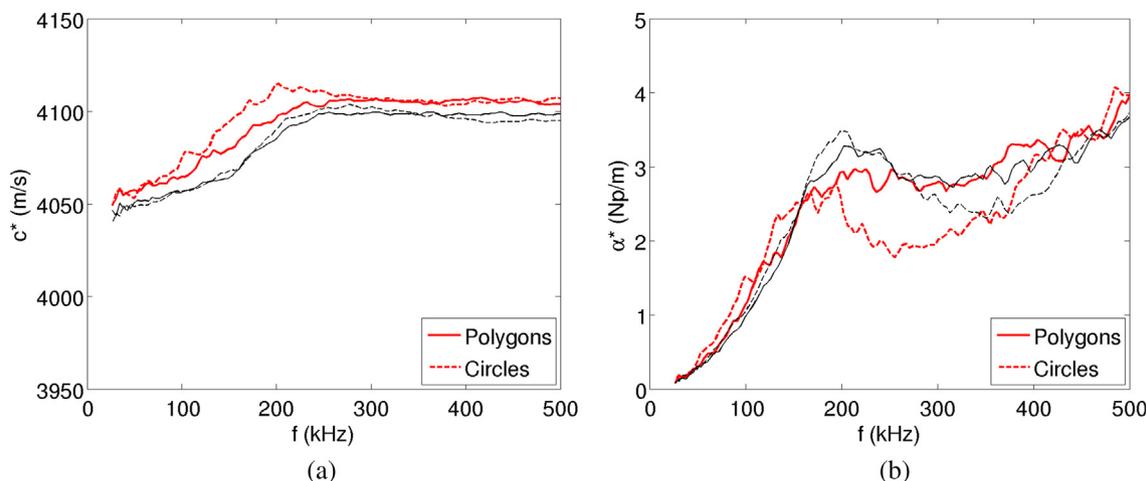
Fig. 14. Comparison of the variations of velocity and of attenuation versus frequency in the case of an incident plane pressure wave propagating in a mortar containing polygons oriented randomly (solid lines) or circles (dotted lines). Two different polygonal shapes are used: with a length over width ratio *l*/*w* of 3–4 at a concentration of 44% (red lines) and with a length over width ratio *l*/*w* of about 2 at a concentration of 42% (black lines).

circles at the same level of scatterer concentration (42–44%): identical radius of 6 mm, and various radii based on three different adaptations for aggregates in VeRCoRs concrete (Fig. 10). In Sections 5.1 and 5.2 they were compared in terms of concentration and in terms of shape. Here we compare them in terms of phase velocity and attenuation in order to highlight the influence of size distribution on wave propagation. The comparisons are shown in Fig. 16. Regarding velocity, the curves are at the same level of amplitude in spite of different shapes of the variations. The three cases at a concentration of 42% (green, blue and black lines) converge towards a similar value of velocity with frequency, while the velocity in the case of a concentration of 44% (red line) is generally slightly greater than the others. Regarding attenuation (Fig. 16(b)), zero, one or two bumps are observed in the evolutions for the four cases, and the locations of bumps depend on size distribution. It seems that attenuation converges to a similar value around 500 kHz. As in the previous cases, attenuation appears to be more sensitive to the size distribution of scatterers.

6. Conclusions and perspectives

In this study, we have built a 2-D plane strain numerical model based on a spectral-element time-domain full-wave software package called SPECFEM2D in order to simulate ultrasonic wave propagation in

concrete, i.e. in a highly heterogeneous medium. After some processing, the simulation results have enabled us to obtain the effective properties of the heterogeneous medium from the averaged coherent field, i.e., to obtain the effective phase velocity and attenuation with respect to frequency.

We validated the numerical model in two steps. First, we compared the numerical results to analytical formulation in the case of scattering by a single circle. Second, the numerical model was then validated by comparing its results to experimental ones obtained with a set of samples made of aluminum rods in resin with increasing scatterer concentration up to 40%, which is representative of applications to concrete. The experimental results obtained for these samples were also compared to the results obtained with two commonly-used homogenization models, the Waterman-Truell and Conoir-Norris models. They were confirmed to be valid and leading to similar results at a scatterer concentration of 5%, and started to fail above (from 20% to 40%).

After that qualitative validation of the numerical model, we used it for parametric studies for applications to concrete. In the case of circular aggregates of identical radius, or of varying radii, at concentration levels of 12%, 24% or 42%, the phase velocity and attenuation were found to increase with scatterer concentration.

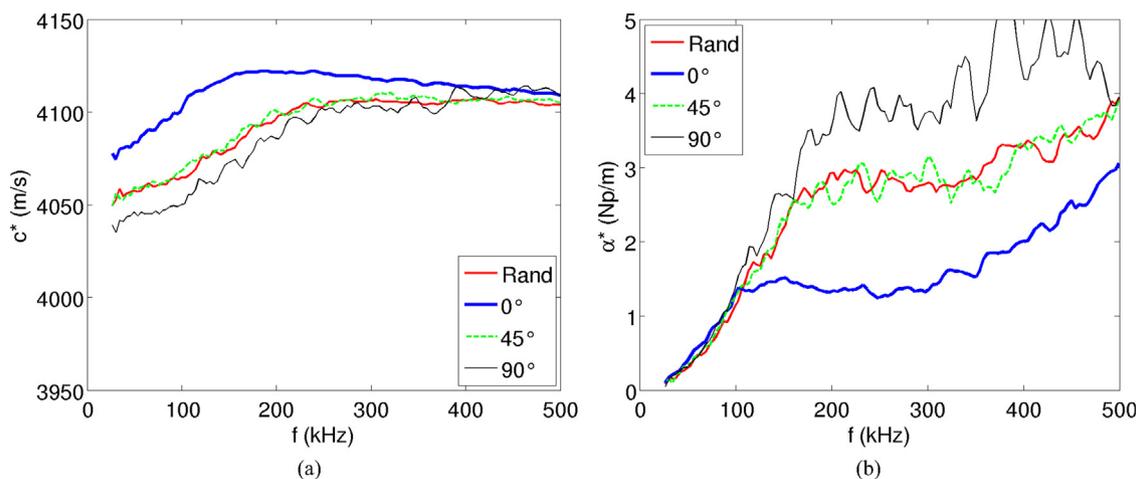When comparing the case of polygonal scatterers with that of

Fig. 15. Comparison of the variations of velocity and of attenuation versus frequency in the case of an incident plane pressure wave propagating in a mortar containing 44% of scatterers of polygonal shape (oriented randomly (red line) or with a privileged direction of 0° (blue line), 45° (green line) or 90° (black line)). (For interpretation of the references to colour in this figure legend, the reader is referred to the web version of this article.)
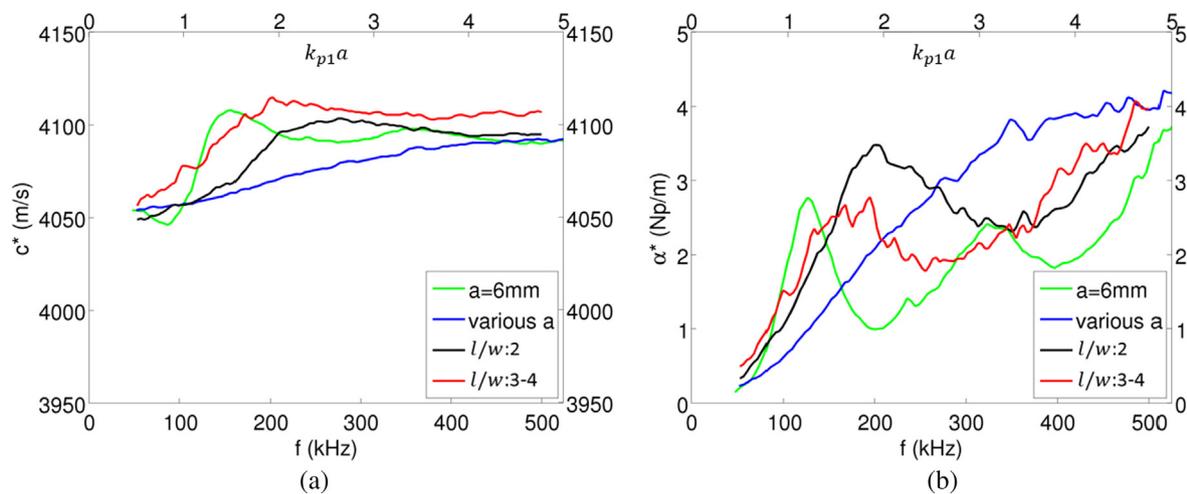
Fig. 16. Comparison of the variations of velocity and of attenuation versus frequency in the case of an incident plane pressure wave propagating in a mortar containing circles of radius 6 mm at a concentration of 42% (green line), circles of various radii at a concentration of 42% (blue line), and circles corresponding to polygons with a length over width ratio l/w of 3–4 at a concentration of 44% (red line) and with a length over width ratio l/w of about 2 at a concentration of 42% (black line). (For interpretation of the references to colour in this figure legend, the reader is referred to the web version of this article.)

circular scatterers, we found little influence on the phase velocity and only a small difference for attenuation if the polygons are randomly oriented. If the polygon shape is not exaggerated, i.e. if the length over width ratio remains below 3 or 4 typically, a shape approximation (simplification) based on circles is thus acceptable.

When comparing the case of polygonal scatterers with and without a privileged direction, a large influence of the privileged orientation was found both for velocity and for attenuation.

In the case of circular aggregates with four different size distributions at the same level of concentration (42–44%), the phase velocity and, especially, attenuation were found to be highly sensitive to the size distribution of scatterers, resulting in the presence or absence of amplitude variations at low frequency for phase velocity, and the presence or absence of bumps for attenuation.

In future work, characterization experiments for mortar corresponding to the VeRCoRs concrete will have to be conducted, and will allow us to take into account the dispersion behavior of mortar (coming from viscoelastic attenuation) in the numerical model. We also think that Interfacial Transition Zones (ITZs) between the mortar and the aggregates should be introduced in the numerical model in order to obtain a more realistic approximation of concrete. Finally, the numerical approach should be used to simulate Non Destructive Testing measurement configurations, so as to better interpret the results and optimize the measuring configurations; in such a case, it will be worth investigating if switching to three-dimensional simulations instead of a two-dimensional plane strain configuration could be necessary.

Appendix A. Supplementary material

Supplementary data associated with this article can be found, in the online version, at https://doi.org/10.1016/j.ultras.2018.07.018.

References

[1] D. Breysse, J.P. Balayssac, S. Biondi, et al., Nondestructive assessment of in-situ concrete strength: comparison of approaches through an international benchmark, Mater. Struct. 50 (2017) 133.

[2] T. Planès, E. Larose, A review of ultrasonic coda wave interferometry in concrete, Cem. Concr. Res. 53 (2013) 248–255.

[3] P. Fröjd, P. Ulriksen, Frequency selection for coda wave interferometry in concrete structures, Ultrasonics 80 (2017) 1–8.

[4] V. Garnier, G. Corneloup, J.M. Sprauel, J.C. Perfumo, Setting time of roller compacted concrete by spectral analysis of transmitted ultrasonic signals, NDT&E Int. 28 (1) (1995) 15–22.

[5] V. Garnier, B. Piwakowski, O. Abraham, G. Villain, C. Payan, J.F. Chaix, Acoustical techniques for concrete evaluation: improvements, comparisons and consistencies, Constr. Build. Mater. 43 (2013) 598–613.

[6] S.O. Naffa, M. Gouygou, B. Piwakowski, F. Buyle-Bodin, Detection of chemical damage in concrete using ultrasound, Ultrasonics 40 (2002) 247–251.

[7] Y.H. Kim, S. Lee, H.C. Kim, Attenuation and dispersion of elastic waves in multiphase materials, J. Phys. D: Appl. Phys. 24 (1991) 10.

[8] L.L. Foldy, The multiple scattering of waves. I. General theory of isotropic scattering by randomly distributed scatterers, Phys. Rev. 67 (1945) 107–119.

[9] M. Lax, Multiple scattering of waves. II. The effective field in dense systems, Phys. Rev. 85 (4) (1952) 621–629.

[10] P.C. Waterman, R. Truell, Multiple scattering of waves, J. Math. Phys. 2 (4) (1961) 512–537.

[11] J.G. Fikioris, P.C. Waterman, Multiple scattering of waves. II. Hole corrections in the scalar case, J. Math. Phys. 5 (10) (1964) 1413–1420.

[12] P. Lloyd, M.V. Berry, Wave propagation through an assembly of spheres. IV. Relation between different scattering theories, Proc. Phys. Soc. Lond. 91 (1967) 678–688.

[13] F. Vander Meulen, G. Feuillard, O. Bou Matar, F. Levassort, M. Lethiecq, Theoretical and experimental study of the influence of the particle size distribution on acoustic wave properties of strongly inhomogeneous media, J. Acoust. Soc. Am. 110 (2001) 2301–2307.

[14] C.M. Linton, P.A. Martin, Multiple scattering by random configurations of circular cylinders: second-order corrections for the effective wavenumber, J. Acoust. Soc. Am. 117 (6) (2005) 3413–3423.

[15] C.M. Linton, P.A. Martin, Multiple scattering by multiple spheres: a new proof of the Lloyd-Berry formula for the effective wavenumber, SIAM J. Appl. Math. 66 (5) (2006) 1649–1668.

[16] R.B. Yang, A dynamic generalized self-consistent model for wave propagation in particulate composites, J. Appl. Mech. 70 (4) (2003) 575–582.

[17] J.M. Conoir, A.N. Norris, Effective wavenumbers and reflection coefficients for an elastic medium containing random configurations of cylindrical scatterers, Wave Motion 47 (2010) 183–197.

[18] Y. Capdeville, L. Guillot, J.J. Marigo, 2-D non-periodic homogenization to upscale elastic media for P-SV waves, Geophys. J. Int. 182 (2) (2010) 903–922.

[19] H. Moulinec, P. Suquet, A numerical method for computing the overall response of nonlinear composites with complex microstructure, Comput. Methods Appl. Mech. Eng. 157 (1–2) (1998) 69–94.

[20] D.J. McClements, Comparison of multiple scattering theories with experimental measurements in emulsions, J. Acoust. Soc. Am. 91 (1992) 849–853.

[21] J.F. Chaix, V. Garnier, G. Corneloup, Ultrasonic wave propagation in heterogeneous solid media: theoretical analysis and experimental validation, Ultrasonics 44 (2006) 200–210.

[22] J.F. Chaix, M. Rossat, V. Garnier, G. Corneloup, An experimental evaluation of two effective medium theories for ultrasonic wave propagation in concrete, J. Acoust. Soc. Am. 131 (6) (2012) 4481–4490.

[23] M. Chekroun, L. Le Marrec, B. Lombard, J. Piraux, Time-domain numerical simulations of multiple scattering to extract elastic effective wavenumbers, Wave Random Complex 22 (3) (2012) 398–422.

[24] K. Nakahata, G. Kawamura, T. Yano, S. Hirose, Three-dimensional numerical modeling of ultrasonic wave propagation in concrete and its experimental validation, Constr. Build. Mater. 78 (2015) 217–223.

[25] D. Komatitsch, J.P. Vilotte, R. Vai, J.M. Castillo-Covarrubias, F.J. Sánchez-Sesma, The spectral-element method for elastic wave equations - application to 2-D and 3-D seismic problems, Int. J. Numer. Meth. Eng. 45 (1999) 1139–1164.

[26] Salome. Retrieved from < http://www.salome-platform.org/ > .

[27] Csimsoft Trelis. Advanced Meshing For Challenging Simulations (2013-2016). Retrieved from < http://csimsoft.com/help/trelishelp.htm > .

[28] F. Schubert, B. Koehler, Numerical time-domain simulation of diffusive ultrasound in concrete, Ultrasonics 42 (1–9) (2004) 781–786.

[29] EDF. The VeRCoRs project. Retrieved from < https://fr.xing-events.com/EDF-vercors-project.html > .

[30] J. Bielak, P. Christiano, On the effective seismic input for non-linear soil-structure interaction systems, Earthquake Eng. Struct. Dyn. 12 (1984) 107–119.

[31] D. Komatitsch, J. Tromp, Introduction to the spectral-element method for 3-D seismic wave propagation, Geophys. J. Int. 139 (1999) 806–822.

[32] T.A. Mokhtar, R.B. Herrmann, D.R. Russell, Seismic velocity and Q model for the shallow structure of the Arabian shield from short-period Rayleigh waves, Geophysics 53 (11) (1988) 1379–1387.

[33] C.C. Mow, Y.H. Pao, Diffraction of elastic waves and dynamic stress concentrations, Crane Russak (1973) 239–274.

[34] Y. Liu, R. Wu, C.F. Ying, Scattering of elastic waves by an elastic or viscoelastic cylinder, Geophys. J. Int. 142 (2000) 439–460.